Article:

eprints@whiterose.ac.uk
https://eprints.whiterose.ac.uk/

Measurement of strain evolution in overloaded roller bearings using time-of-flight neutron diffraction

A. Reid [a,*], M. Marshall [a], I. Martinez [a], S. Moorby [b], T. Connolley [c], M. Mostafavi [d], S. Kabra [b]

[a] University of Sheffield, Dept. Mechanical Engineering, Sheffield S1 3JD, UK
[b] STFC-Rutherford Appleton Laboratory, ISIS Facility, Harwell OX11 0QX, UK
[c] Diamond Light Source Ltd, Harwell Science and Innovation Campus, Didcot, Oxfordshire OX11 0DE, UK
[d] University of Bristol, Dept. Mechanical Engineering, Bristol BS8 1TR, UK

HIGHLIGHTS

- Time-resolved elastic strains were measured in an operational roller bearing using a specially designed dynamic loading rig.
- Time-of-flight neutron diffraction was used to measure strain under different static loads.
- Dynamic testing showed increasing subsurface compressive strain, indicative of material softening.
- Eventmode data acquisition permitted evaluation of cyclic strains associated with rolling contact fatigue.
- Evidence of surface and subsurface failure was observed post-mortem using confocal scanning and optical microscopy.

GRAPHICAL ABSTRACT
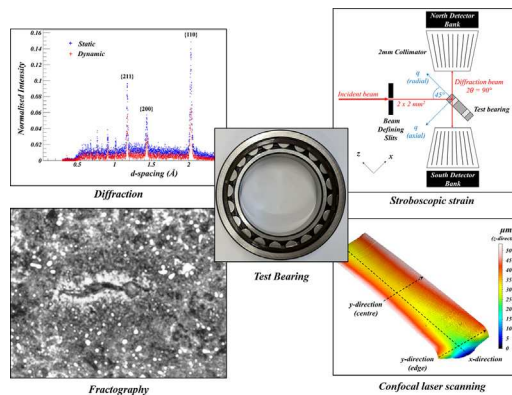
ARTICLE INFO

ABSTRACT

Neutron diffraction is an established method for non-destructively characterising residual stress or observing in situ strain during external stimuli. Neutron based stroboscopic techniques have previously been introduced for measuring strains undergoing cyclic processes but have not been used for tribological applications. This work presents a novel approach for measuring the evolution of radial strain in a rotating bearing through part of the component's lifetime. A cylindrical roller bearing was pre-overloaded to increase the probability of damage within a reasonable experimental time and to help develop further understanding of the influence such events have on bearing life, notably for the application of wind turbine gearbox bearing failure. The stroboscopic neutron diffraction technique was successful in measuring time-resolved contact strain, with a significant increase in compressive radial strain being observed after a suspected failure had been detected using condition monitoring techniques, implemented for validating damage propagation. Cyclic contact strains associated with rolling contact fatigue were also evaluated using neutron diffraction.

* Corresponding author.
E-mail address: agpreid1@sheffield.ac.uk (A. Reid).

1. Introduction

1.1. Background

Power generation from sustainable sources is of extreme importance, with global renewable energy capacity increasing by roughly 257% between 2008 and 2017 [1]. Wind power has played a significant role in the growth of renewable energy generation, yet premature failure of wind turbine components is proving to be an issue for the industry [2]. Operation and maintenance of wind turbines is challenging and costly, as the unexpected failure of a critical drivetrain components normally leads to significant downtime. The failure of a wind turbine gearbox (WTG) bearing can suspend operation for up to 23 days [3], suggesting that a deeper understanding of WTG bearing failure mechanisms is essential for improving wind turbine reliability [4].

The mechanisms responsible for premature WTG bearing failure vary and more appreciation for the influence of non-torque loading may be required for future gearbox design, as this effect can lead to highly transient contact pressures [5]. Recently several test rigs have been designed to study the effect of non-torque loading on WTGs, with the aim of understanding and optimising commercial gearbox lifetime [6]. The impact of WTG bearing overloads, in which contact pressures exceed the material's yield strength, has been highlighted as one potential cause of accelerated failure in these components [7]. It has been suggested that wind conditions associated with underloading, whereby surface damage developing through excessive skidding and wear, are more prevalent than overload events. In reality, one or a combination of both phenomena may contribute towards damage [8]. Overloads are the result of inertial effects along the WTG drivetrain caused by instantaneous impulses from transient wind conditions, torque reversals when engaging and disengaging from the grid or misaligned drivetrain components [9]. Previous work has demonstrated that overloading generates regions of subsurface plasticity, which may significantly reduce bearing life expectancy [10].

Gross plastic deformation in bearings is strongly linked with severe distortion of microstructure, potentially accelerating the formation of subsurface failure processes, for example white etching cracks (WECs) [11]. WECs are associated with rolling contact fatigue (RCF) and have been intensely researched [12,13]. Whilst a definitive cause for this phenomenon remains unknown, WECs are frequently observed encompassed by a white etching area (WEA). 'White etching' refers to a white appearance of localised microstructure when observed under an optical microscope post-etching. It has been proposed that WEAs generate as the result of carbide dissolution through exposure to cyclic stresses during RCF, leaving a region of nano-ferrite grains supersaturated with carbon, 30–50% harder and more brittle than the surrounding steel matrix [14,15]. It is common for bearing applications that WEA and WECs occur near to material inclusions, referred to as butterflies due to their appearance [16]. Dark etching regions (DER), named due to the dark appearance of the deformed microstructure, are more uniform subsurface features and have low hardness when compared to the surrounding matrix [17]. Previous studies have suggested that DERs occur prior to WEC nucleation and are indicative of the early stages of RCF initiated failure [18,19]. It was demonstrated that the size of DERs generated during RCF resembled the plastic zone geometries predicted using elastoplastic modelling [20]. This implies that significant overload events can create a large subsurface region that is susceptible to RCF damage, with subsequent cyclic contact stresses occurring within the deformed area.

1.2. Engineering neutron diffraction

Neutron diffraction provides the unique opportunity to non-destructively probe materials, measuring internal elastic strains and thus allowing for calculation of stresses. Strain diffractometry involves measurement of the interplanar lattice spacings within crystalline materials, with the planes effectively acting as atomic-scale strain gauges. A significant advantage of neutron diffraction techniques, particularly when compared to X-ray diffraction, is that neutrons have higher penetration powers in engineering materials, such as steel [21].

A time-of-flight (ToF) neutron source produces a pulse of polychromatic neutrons through a spallation process. Incident neutrons are guided towards the sample, interact with the material and diffract at an angle dependent on their energy [22]. For a neutron ToF strain diffractometer the detectors are generally at a fixed location, usually measuring diffraction angles of $\pm 90°$ to the incident beam [23]. The experimental gauge volume is defined as the region situated at the incident and diffracted beam intersection [22]. The incident beam geometry is selected using aperture slits and diffracted beam geometry determined through collimation [24]. Neutron flight paths, from the spallation target/moderator assembly to the instrument detectors, via the sample gauge volume, are fixed and well-defined, with the ToF entirely dependent on individual neutron energies. Wave-particle duality states that the neutrons will have a wavelength associated with energy, meaning that Braggs law can be used to calculate the average interplanar lattice spacing within the experimental gauge volume. Eq. 1 demonstrates the calculation for interplanar lattice spacing, or d-spacing (d_{hkl}), using neutron ToF information [25]. For a value of $2\vartheta = 90°$, the neutron scattering vector direction, q, and therefore measured strain component will be at 45° to the incident and diffracted beams.

$$d_{hkl} = \frac{h\,ToF}{2\,m\,L\,sin\vartheta} \tag{1}$$

where, h is Plancks constant, m is the neutron mass, L is the flight path from moderator to detector and ϑ is the angle between the incident beam and the scattering vector. The detected spectrum, or diffraction pattern, is a plot of neutron intensity as a function of ToF or d-spacing, and usually consists of several peaks, each corresponding to a specific family of {hkl} lattice planes. Elastic strain can be calculated using changes to the interplanar spacing, observed as a shift in peak position, relative to a stress-free value, d_{hkl}^0 (Eq. 2) [23]. Fig. 1 demonstrates the exaggerated peak shift expected during compressive loading. Once a diffraction pattern has been acquired, there are two approaches for obtaining macroscopic strains, namely single peak fitting or full pattern fitting. Using single peak fitting, provides the strains relating to a specific crystallographic plane, d_{hkl}, whilst full pattern fitting gives strains relating to changes in the overall lattice parameter, a. The latter being
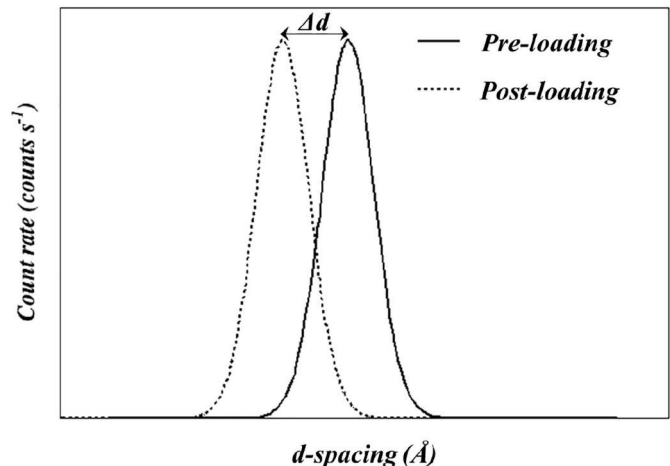

Fig. 1. Exaggerated peak shift in a generic Bragg peak, demonstrating the effect of compressive loading..

$$\varepsilon_{hkl} = \frac{d_{hkl} - d_{hkl}^0}{d_{hkl}^0} = \frac{\Delta d_{hkl}}{d_{hkl}^0}, \varepsilon_{bulk} = \frac{a - a_0}{a_0} = \frac{\Delta a}{a_0}$$

an average, make it more representative of the macroscopic strain state. The least-squares procedures, Rietveld and Pawley refinement, are the preferred techniques for full pattern fitting [26,27]. The resulting value of a can be then used to calculate strain using a stress-free reference lattice parameter, a_0, analogous to d_{hkl}^0 for single peak fitting, as seen in Eq. 2.

Traditionally, engineering neutron diffraction experiments involve the characterisation of residual or in situ strain. Common residual stress measurements include those performed on welded or cladded specimens [28,29]. Narayanan et al. successfully measured residual stresses in a laser cladded rail, demonstrating the benefits in reducing the effect of ratcheting under fatigue loading and consequent wear mechanisms [30]. The study additionally highlights the benefits of neutron diffraction as a complementary technique for measuring residual stress, potentially being used in parallel with semi-destructive procedures, such as incremental hole drilling. In situ neutron experiments generally involve the measurement of strains within a sample under varying load, occasionally during exposure to harsh high-temperature or cryogenic conditions [31,32]. For example, in situ neutron diffraction has been used to characterise the stress relaxation of Inconel 625 nickel-base superalloy at temperatures of 700 °C, comparing behaviour of conventionally processed and additively manufactured specimens [33]. It is common practice to apply neutron diffraction results for validating computational models, such as Finite Element Analysis (FEA) [34].

A disadvantage of neutron diffraction is the relatively long data acquisition times that are required to collect suitable statistics for performing the peak fitting procedures, particularly compared to rapid X-ray data acquisition rates. Depending on the gauge volume geometry, it can take between a few minutes and a few hours to obtain sufficient neutron counts for steel, with smaller gauge volume's requiring longer scan times [25]. Nonetheless, if the stress state within the specified gauge volume remains constant throughout the measurement, for example during residual stress characterisation, this does not pose much of a problem. However, if stress conditions are continually altering throughout data acquisition then the accuracy of measurements will be compromised, making time-resolved studies more difficult. As a result, the development of stroboscopic techniques has been used as a method for measuring the time dependent variation of strain in cyclic processes [35].

Stroboscopic measurements are useful for measuring cyclical processes where the strain state varies within each cycle but every cycle is nearly the same. Even though the neutron statistics within each section of the cycle is insufficient for a full analysis, if the same section of the cycle is added up over multiple cycles, enough statistics can be obtained for the data to be analysable. Stroboscopic strain measurements using neutron diffraction were introduced in 1996, to study the behaviour of a metal matrix composite exposed to thermal cycling [35]. The composite was rapidly cycled between 175 and 400 °C, with a reference signal being sent from the furnace to the data acquisition system at the beginning of each cycle. There have since been several stroboscopic neutron experiments, including a study by Feuchtwanger et al. which used a reference pulse generated from an Instron loading frame to synchronise neutron data acquisition with the applied strain, allowing for the study of stress-strain behaviour in polymeric matrix composites [36]. The loading frequency for this experiment was 0.5 Hz, using 100 time segments for every individual cycle, with each segment being 20 ms. Furthermore, a recent study also successfully measured time-resolved strain in a piezoelectric actuator, exposed to an alternating electric field of frequency 0.5 Hz and magnitude of 0–130 V [37]. Neutron detection events were divided into 26 segments each with a width of 10 V, allowing for the evaluation of cyclic strains. It is apparent from these previous studies that to successfully measure time-resolved strain a suitable triggering system is required, in order to provide a reference for data acquisition processes.

Stroboscopic X-ray experiments are more commonplace due to rapid data acquisition rates, with Baimpas et al. using the technique to measure dynamic strain in the connecting rod of an operational internal combustion engine [38]. Time-resolved X-rays were also used for tribological applications, to measure dynamic contact strain in a ball bearing, using a Hall sensor to trigger whenever a ball passed the region of interest [39]. A more recent study used a fibre optic triggering system to detect every individual roller passage in a rotating bearing. This method was capable of performing dynamic strain measurements in under 13 min, with a contact loading frequency of 125 Hz associated with bearing operation at 854 *rpm* [40]. The equipment from the mentioned X-ray experiment has been adapted for stroboscopic neutron diffraction experiments, forming the basis of the present study.

1.3. Aims and structure

The aims of this study are to (i) develop hardware and software for measuring dynamic contact strain using ToF neutron diffraction, (ii) stroboscopically measure dynamic in situ elastic strain in an overloaded roller bearing, (iii) develop a method for processing stroboscopic data to obtain cyclic strain associated with rolling contact fatigue, (iv) develop further understanding of the influence overloading has on bearing failure.

Using a novel stroboscopic triggering technique and utilising the benefits of eventmode neutron data acquisition systems, it has been demonstrated that there is potential for measuring dynamic strain, even at the high rates of strain variation experienced at the contact of an operational roller bearing. A loading rig was designed for the purpose of conducting dynamic strain measurements on a running bearing using the ENGIN-X neutron diffractometer. Stroboscopic neutron diffraction has successfully been used to study the evolution of strain at the maximum stress state, as well as characterising cyclic strain variation associated with rolling contact fatigue. This work offers a novel approach in the field of tribology to further understand RCF using time dependent strain measurements, whilst results support the hypothesis that overloads accelerate raceway damage, lowering bearing life expectancy, with post-test interrogation confirming the occurrence of surface and subsurface damage.

2. Experimental design

2.1. Test bearing

The experiment was designed to be performed using both energy dispersive X-ray diffraction and ToF neutron diffraction, however this body of work focuses on results obtained during the neutron investigation. The test bearing was selected with major consideration given to the sample geometry, optimising radiation attenuation, particularly for X-rays, as neutrons penetrate AISI 52100 bearing steel more easily. The SKF NU1010 ECP cylindrical roller bearing was selected, as a raceway thickness of 16 mm ensured up to 9% transmission for high energy X-rays, allowing for penetration that provides suitable data acquisition [40]. The bearing has 20 rolling elements with an outer diameter, D, and bore diameter, d, of 80 mm and 50 mm, respectively (see Fig. 2b). As WTG bearings are very large components, they would be unsuitable for diffraction experiments due to attenuation issues, nonetheless the test bearing recreates similar operational contact pressures to those generated in a commercial WTG, whilst being scaled down appropriately in size. A cylindrical roller bearing creates a line contact between roller and raceway, generating subsurface stress fields that are inherently less complex that those associated with point contacts found with spherical rolling elements. This allows for the assumption that stresses are uniform in the axial direction (x-axis), along the contact. Table 1 contains the chemical composition, whilst Table 2 shows the material properties of AISI 52100 bearing steel.
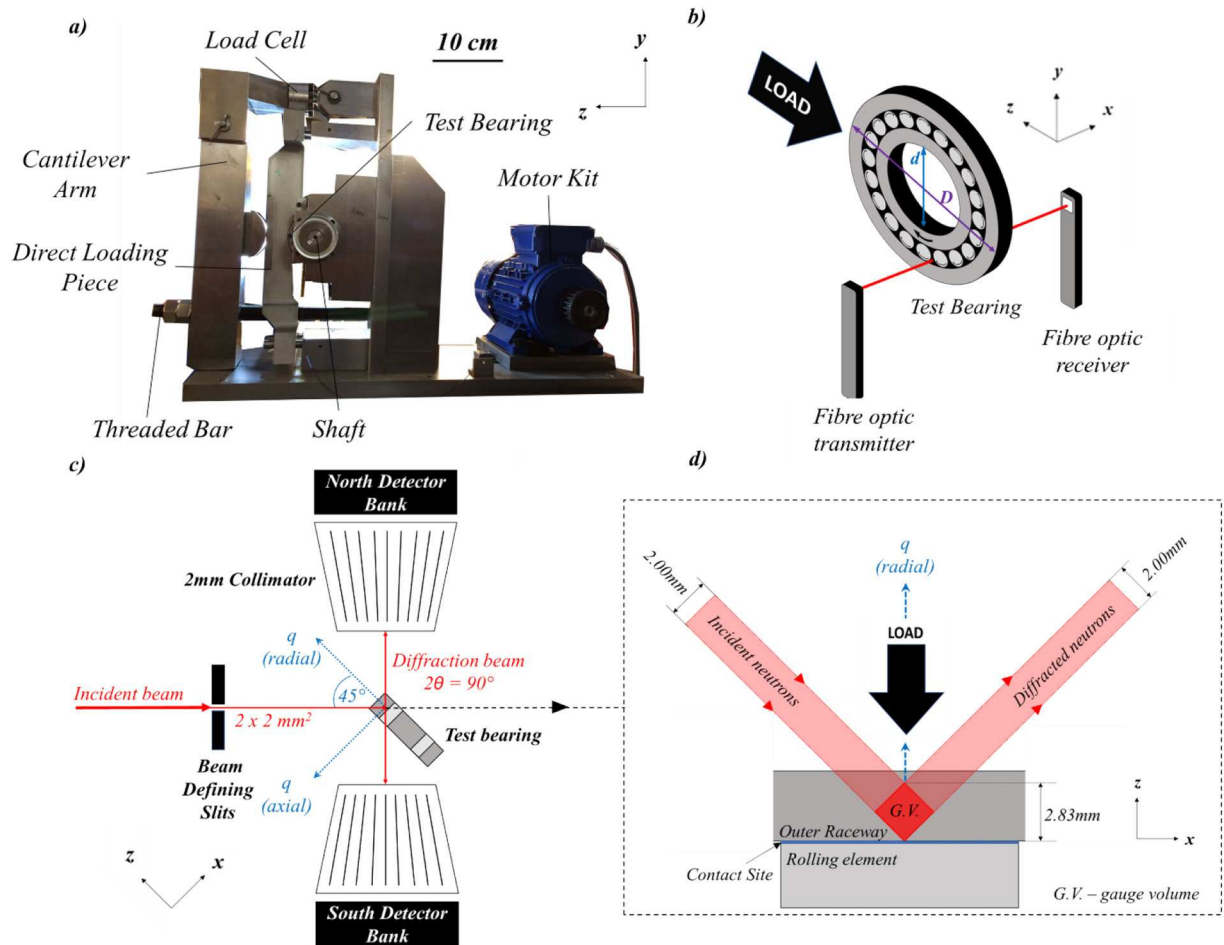
Fig. 2. a) Photograph of the dynamic loading rig. b) Fibre optic system used for the stroboscopic strain measurement technique. c) Schematic of ENGIN-X experimental setup. d) Projection of the cubic gauge volume in the xz-plane.

2.2. Dynamic loading rig

A purpose-built rig was designed with essential features, taking into consideration that experimentation was to be performed using both the I12 X-ray beamline and the ENGIN-X neutron strain diffractometer, each with unique setup requirements and scattering geometries [25,43]. Further details on the features that are specific to the X-ray experiment are included in previous work [40]. Detector geometry (fixed ±90°) at ENGIN-X allows for a maximum of two orthogonal strain components to be measured simultaneously. Since the radial component (z-axis) was of primary interest, only that component was measured in the presented work. The rig was designed to apply loads and perform neutron measurements along a direction of 90° from the top of the rig, ensuring that the neutron scattering vector was aligned with the bearing radial loading direction. Fig. 2a, shows a photograph of the rig.

The rig was fitted with an OMEGA LCM20-20kN load cell and SGA/A load cell amplifier, with loads applied using a cantilever arm and threaded bar screw mechanism. A direct loading piece (DLP), between the cantilever arm and the test bearing, was guided by linear ball bearings to ensure that load application was radially aligned. Care was taken to ensure that rig components did not obstruct the incident and

diffracted neutron beam line-of-sight, yet this could not be avoided with the DLP. Therefore, the DLP was constructed with aluminium, which has a very low neutron absorption cross-section (0.23 b for aluminium compared to 2.56 b for iron with neutrons at 2200 ms^{-1}), thus making it effectively transparent at this material thickness [44]. There were also access points made available for the mounting of acoustic emission sensors (AE) and accelerometers, as part of a condition monitoring project running in parallel with this study [45].

2.3. Neutron diffraction strain measurements

The experiment was completed on the ENGIN-X neutron strain diffractometer at ISIS Neutron and Muon Source, UK [25]. The ENGIN-X beamline is a designated engineering strain scanning instrument, with a neutron flight path of approximately 50 m and high flux over a wavelength range of 1–3 Å, suitable for most polycrystalline engineering materials. A neutron pulse rate of 25 Hz was used, providing a ToF window for each individual pulse of approximately 40 ms. The rig was positioned on the sample stage with the bearing z-axis at 45° to both the incident

Table 1
AISI 52100 chemical composition (wt%) [41].

C	Mn	Si	Cr	Cu	S
0.95–1.10	0.20–0.50	≤0.35	1.30–1.60	≤0.025	≤0.025

Table 2
AISI 52100 Properties [42].

Property	Symbol	Value
Density [kg/m^3]	ρ	7827
Young's Modulus [GPa]	E	201
Poisson's ratio	ν	0.3
Yield Stress [MPa]	σ_Y	1410

neutron beam and north detector bank, allowing for measurement of the radial strain component. Fig. 2c shows a schematic of the sample in relation to the neutron beam and scattering vectors. The slits were opened to allow for an incoming beam with a cross-section of 2×2 mm^2, whilst the 2 mm collimators were positioned in front of the detectors to limit the diffracting volume in that direction. This resulted in a $2 \times 2 \times 2$ mm^3 gauge volume, aligned with the overloaded region of interest in the raceway subsurface, as represented in Fig. 2d, where it should be noted that the cubic gauge volume sits 45° to the bearing coordinates. Scans were also performed on standard calibration samples; vanadium and NIST standard cerium oxide. Cerium oxide is a very strong coherent neutron scatterer, with well-defined lattice parameters, allowing for ToF information to be accurately calibrated. The vanadium sample is a very poor coherent neutron scatterer but a strong incoherent scatterer, used to determine the incoming incident neutron spectra. This is then used to normalise the collected experimental data.

The experiment included static scans (stationary bearing), typical of those performed during ENGIN-X experiments, and dynamic scans, which required a stroboscopic method for synchronising the bearing rotations with the ENGIN-X data acquisition electronics (DAE). Static scans were performed without shaft rotation and with a roller placed in contact with the outer raceway location being measured. The gauge volume was positioned in the outer raceway, directly beneath the rolling element contact, allowing for the measurement of subsurface elastic radial strain under different loads, P_s. Static scans were performed for 28 min each at increasing increments of $P_s = 10$ kN up to 40 kN, with the stress-free a_0 lattice parameter measured at 0 kN, allowing for calculation of relative elastic strain. A maximum load of 40 kN was selected because it had previously been demonstrated as being slightly within the elastic limit, according to FEA, described in Section 2.5.1.

Dynamic scans were performed, measuring strain in an overloaded region of the static outer raceway, while the bearing was running at 927 rpm under a constant radial load of $P_s = 40$ kN. Overloads were performed using a fixed raceway loading frame (FRLF), described in previous work [10]. The frame uses a single isolated rolling element mounted in a static shaft, with a fork mechanism used to apply the designated load to a fixed outer raceway. Loads are applied using an Instron loading frame, meaning that the FRLF can also be used for 'static fatigue' investigations, with such results presented in Section 3.4. An overload equivalent to $P_s = 136$ kN was applied prior to the dynamic test, with subsurface plasticity propagation reaching the contact surface, as predicted the FEA. The substantial overload maximises acceleration of damage and increases the likelihood that failure will be observed during the experiment.

For dynamic strain measurements, a stroboscopic triggering technique was used, as previously described in the stroboscopic X-ray study [40]. This made use of a Keyence FU-18M thru-beam fibre optic system to detect the passage of individual rolling elements (Fig. 2b). For every roller passage the Keyence FS-N10 Series digital amplifier generated a PNP (positive, negative, positive) output signal, which was converted to a TTL (transistor-transistor logic) pulse using a Stanford Research Digital Delay/Pulse Generator. The TTL pulse triggered a Phantom 7.3 high speed camera, used to capture a still image of the region of interest, ensuring that the roller was in contact with the overloaded zone on the rising edge of the pulse, after correcting for a time delay. The high speed camera was used to determine the delay.

The delayed TTL pulse was used to provide a time-reference, indicating where the rollers were positioned throughout the experiment. The delay/pulse generator was used to specify a pulse width (Δt), which determines the size of the time-bins used for filtering neutrons. The reference pulse was fed into the DAE to synchronise roller position with the detection of the ToF neutrons. The DAE consisted of a Digital Data Interface Board, which fed into the Sample Environment Breakout Board (SEBB) and the detector card. The DAE was operated in eventmode for dynamic tests. The fibre optic pulse metadata from the sample

environment, could be logged using an analogue-to-digital converter (ADC) channel in the SEBB, along with neutron detector acquisition running in synchronisation. Whilst running in eventmode, every neutron detection is stored with the time of collection, allowing for filtration of these events into discrete time-bins during post-processing.

In the raw eventmode data, each recorded neutron event corresponds to a neutron reaching the detector, rather than a neutron reaching the sample. In order to ensure the recorded events relate directly to the time at which the neutron is at the sample, a time shift has been applied to each individual event timing, using a custom-made Mantid script. Eq. 3, derived using de Broglie's equation, has been used to calculate the time shifts that have been applied to the neutron events, with the shift being a function of the individual neutron wavelength.

$$s = -\frac{L_d \, m \, \lambda}{h} = -\frac{\lambda}{2.6373} \tag{3}$$

where, s is the time shift in ms, L_d is the distance between the sample and detector pixels (1.5 m on ENGIN-X) and λ is the neutron wavelength measured in Å. For slower cyclic processes, for example below 10 Hz, this effect can be ignored. However, in this case the time required for the neutron to reach the detector after scattering is comparable to the cycle times and therefore needs to be considered.

Each eventmode data file consisted of roughly 28 min of data acquisition, rather than storing data in one continuous file, which would be too large for post-processing. Fig. 3 provides an example of an ADC sample log recording, indicating a time period of 7.56 ms, or BPF of 132 Hz, validating the predicted outer raceway BPF$_o$ of approximately 136 Hz for a shaft speed of 927 rpm, using Eq. 4 [46].

$$BPF_o = \frac{\omega_s \, z}{120} \left(1 - \left(\frac{d}{D} \right) \cos\alpha \right) \tag{4}$$

where, ω_s is the shaft speed in rpm, Z is the number of rolling elements, d is the rolling element diameter, D is the bearing pitch diameter and α is the contact angle between the roller and the raceway.

2.4. Stroboscopic data analysis — dynamic scans

Eventmode data was analysed using python scripting, which incorporated pre-programmed algorithms within the Mantid Project Application Programming Interface [47]. In order to analyse data collected whilst the DAE was operating in eventmode, the ADC sample log is required to generate a filter workspace, consisting of a sequence of start and stop times corresponding to the beginning (t_0) and end of an individual pulse ($t_f = t_0 + \Delta t$). All filter times are determined using a threshold value in the sample log, in this case the threshold was set to 2200 mV, capturing the rising edge of each pulse (see Fig. 3).

The neutron detection events and the filter workspace events generated from the roller passage are all synchronised with the same clock, relative to the start of the individual scan. A separate algorithm then collates all the neutron events that occurred at times between the t_0 and t_f, for each roller passage throughout the entire scan. These neutrons are then re-collated to generate a diffraction spectrum, like those generated by the DAE during static scans. The ToF resolution for both static and dynamic data was set to 4.67 μs.

As every neutron acquisition is recorded, with their individual ToF information, the reference pulse generated as a roller passes the region of interest can be shifted to evaluate the cyclic variation of strain during bearing operation, demonstrated by the inset of Fig. 3. As the pulse width was one-seventh of the time period, neutrons were segmented into seven time-bins, each equal to the pulse width. Therefore, every recorded neutron incident was used to generate a spectrum for fitting strain data. Consequently, the statistical quality of data associated with a single scan was compromised by splitting the neutron counts, but to
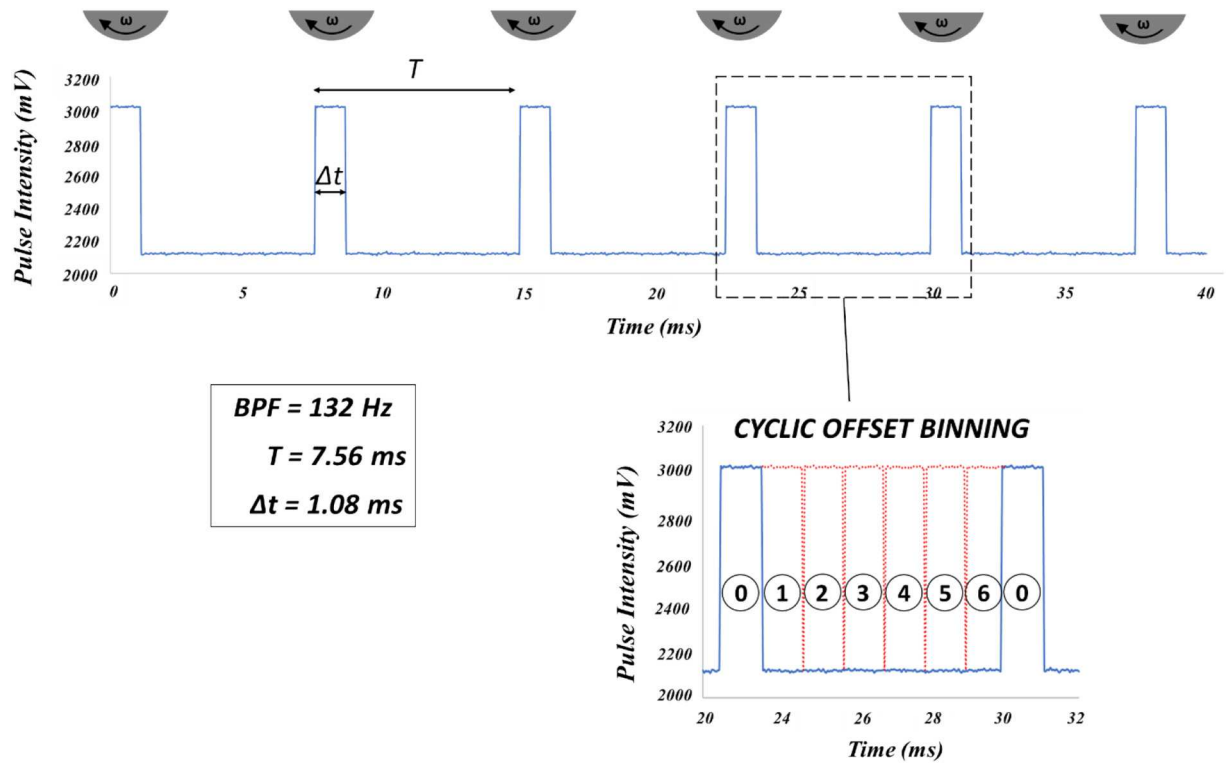
Fig. 3. ADC sample log reading demonstrating the generation of pulses over 40 ms, the ToF range recorded for each pulse of neutrons. INSET – visualisation of the seven time-bins (numbered with an index starting at zero) generated by shifting the original pulse by an integer multiple of the pulse width.

minimise this effect four scans were merged together during post-processing, providing suitable quality of statistics for fitting. Merging was performed using a running average with successive overlaps, so as not to significantly reduce the number of strain values generated over the entire experiment. This resulted in nearly 2 h of data collection to produce each fitted strain measurements.

In order to obtain the lattice parameters, all spectra, static and dynamic, were fitted using the GSAS-II crystallography software [48],
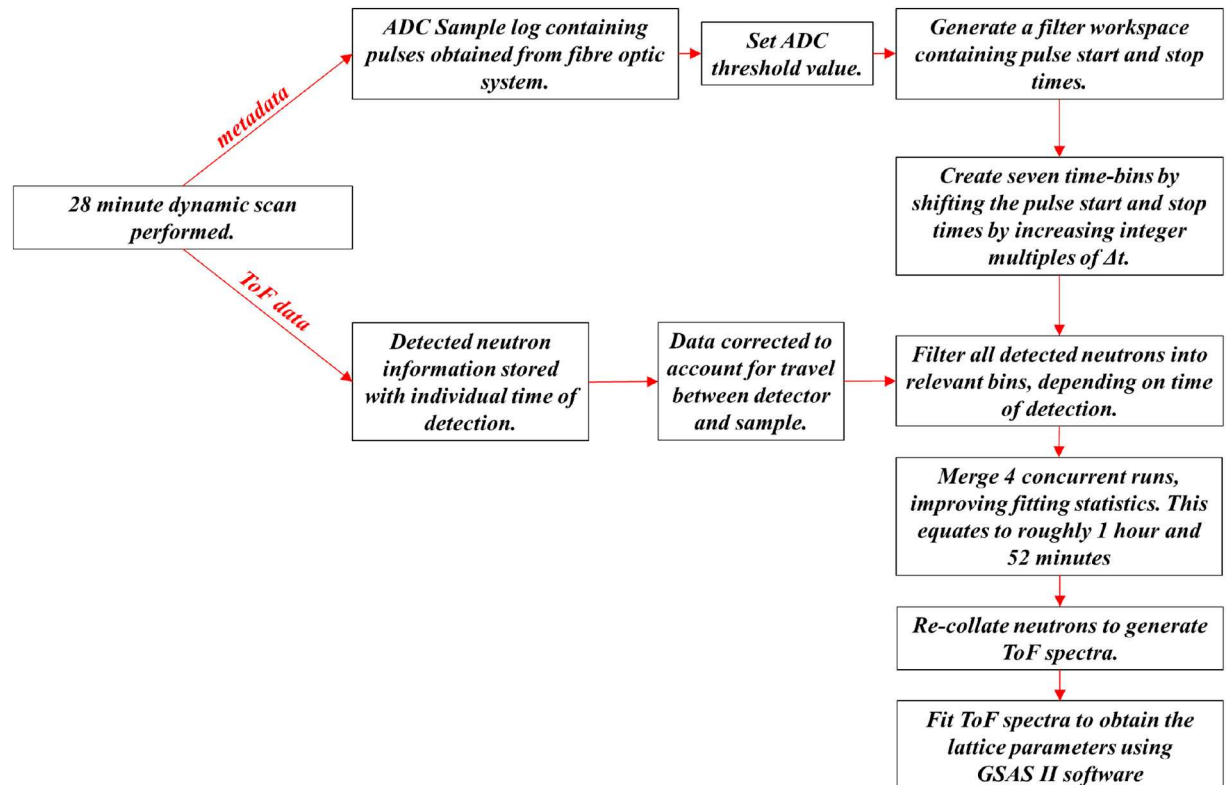

Fig. 4. Summary of the processing steps for dynamic scans.

with Pawley refinement in the ToF range of 20 ms and 40 ms (d-spacing range of 1.09 Å to 2.17 Å), incorporating the most prominent {110}, {200} and {211} Bragg peaks. Fig. 4 presents a graphic, summarising the individual processing steps for dynamic scans. Fig. 5 shows a comparison between the static and dynamic data. The peak intensities and counting statistics are greater for the static scans, as would be expected due to dynamic data post-processing techniques reducing the effective data acquisition time. The average strain uncertainty, obtained from errors in the fitting procedure, was ±93 με for static scans, whereas for dynamic scans the average uncertainty was ±108 με, verifying that data is of better quality for static data collection. Single peak analysis was attempted using the {211} plane, yet fitting errors were higher than those from using multi-peak analysis. To obtain sufficient statistics for single peak fitting, a greater number of scans would need to be merged, reducing overall time resolution.

2.5. Modelling

2.5.1. Finite element analysis

In a previous study, FEA simulated in ABAQUS version 6.14-2 [49], was used to predict the elastic and plastic behaviour of the sample. The primary aim of the model was to provide the loading conditions whereby the elastic limit was exceeded and the extent of subsurface yielding that occurs during overload. The model was validated using Hertzian contact theory, showing excellent agreement with the calculated theoretical predictions of contact pressure and elastic load limit [10]. A schematic of the three-dimensional elastic-plastic model, with boundary conditions, is demonstrated in Fig. 6. Quadratic elements (C3D20R) were used for modelling the bearing raceway and roller element, whilst the remaining components were bilinear rigid quadrilateral elements (R3D4). Contact friction was assumed to be negligible as static loading conditions were being simulated, whilst only one-quarter of the bearing was modelled to reduce computational expense, with symmetry assumed in the x-axis and ϑ-axis. Additionally, isotropic hardening was assumed using derivations from the AISI 52100 stress-strain curve [50]. Table 2 provides the AISI 52100 material properties used for the model.

2.5.2. Analytical raceway model

Hertzian contact theory was utilised for comparison of the subsurface elastic strains being generated in the raceway at different static and dynamic loads [51]. For comparison with static scans, two-dimensional subsurface strain fields were calculated, in the yz-plane, for each experimental load. As a line contact was generated between the roller and the raceway, strains were assumed to be uniform along

the contact (x-axis). This assumption allows for averaged strains within a theoretical three-dimensional gauge volume to be obtained by weighting the calculated two-dimensional strain field, as the orientation of the cubic gauge volume, relative to the sample, is known. The experimental gauge volume extended to a depth of 2.83 mm into the subsurface, due to detector geometry and beam alignment with the sample, as demonstrated in Fig. 2d. Note that Fig. 2d and Fig. 7 present the gauge volume as viewed from the xz-plane and yz-plane, respectively.

For dynamic strains, traction between the roller and the raceway surface was incorporated by the model, assuming that Amontons' law holds [52,53]. A coefficient of friction of 0.05 was assumed, which is relatively high for most roller bearing applications, yet has been demonstrated to be reasonable for very high loads, such as those being used in dynamic test ($P_s = 40$ kN) [54]. The model simulated a static bearing raceway, with subsurface radial strains generated as rollers moved throughout the period of a single roller passage, T, relative to when a roller was in contact with the contact site beneath the gauge volume, where t = 0. Fig. 7 demonstrates the model at t = 0, t = T/3 and t = 2 T/3, with the 2 × 2.83 mm cross-section of the gauge volume represented with a black box.

2.6. Novelty detection

A novelty detection strategy was implemented to determine whether bearing damage was produced during operation. A common strategy includes comparing the vibrational spectral data obtained from the acceleration signal to identify the occurrence of any peaks at the characteristic defect frequency, relating to a specific bearing component. In practice, this type of analysis may not always be possible and thus more sophisticated methods are needed to provide a reliable diagnosis.

The vibrational data was measured with a tri-axial acceleration sensor (PCB 356B21), bonded on the top of the rigs DLP using a cyanoacrylate. The output was connected to a NI cDAQ 9223 Module coupled to a NI cDAQ 9184 chassis for signal acquisition. The rig was monitored via a LabVIEW interface that allowed visualisation of the captured signal in real time and to perform basic storage operations. The recorded signal was periodically stored by segmenting 10 s streams of data every 15 min at a sampling rate of 51.2 kHz.

In order to find any deviation from the bearings standard operational behaviour, a novelty detection method based on the Squared Mahalanobis Distance (SMD) was used. This method quantifies the extent that a measured point differs from the standard conditions in terms of standard deviations with respect to a specific distribution. Therefore, if a measured multidimensional feature shows a greater separation between a specific distribution representing the normal (undamaged) state of the machine, then a novelty can be inferred. The SMD can be defined using Eq. 5.

$$D_\varsigma = \sqrt{(x-\mu)\Sigma^{-1}(x-\mu)'}\#$$

(5)

where x, μ and Σ^{-1} represent the n-dimensional sample point, the mean and the inverted covariance matrix respectively. The analysed features were vectors containing spectral data obtained from the vertical axis of the acceleration signal. These features were obtained by transforming the time domain acceleration signal, using the Fast Fourier Transform algorithm, and then reduced to a frequency range of 25 to 150 Hz. This method requires a baseline feature, used as a reference for the undamaged state, and obtained by calculating the mean and covariance matrix for a pristine bearing sample. Findings from the novelty detection approach for condition monitoring are detailed further in work completed by Martinez et al. [45].
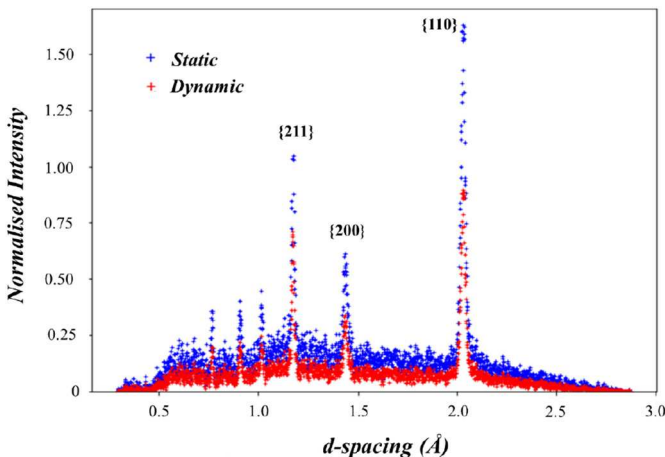

Fig. 5. Comparison of static and processed dynamic spectra normalised using a vanadium standard sample.
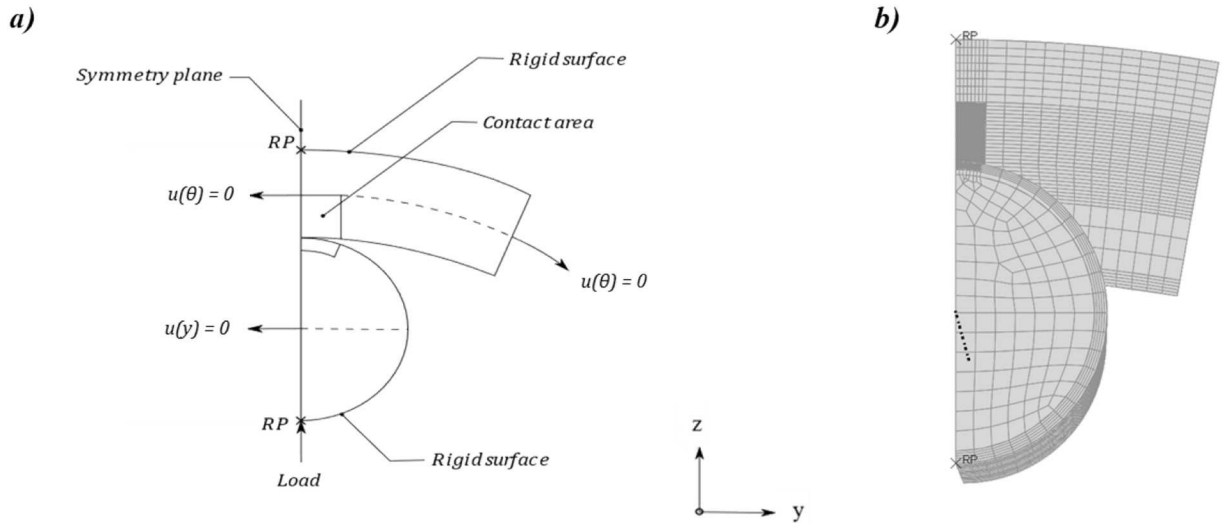
a)

b)

Fig. 6. a) Finite Element Model boundary conditions. b) Mesh.

3. Results

3.1. Static strain measurements

Strains measured during static scans are presented in Fig. 8, alongside values predicted by Hertzian contact theory. The elastic compressive strain increased with load application, yet at lower loads there was lesser agreement with the analytically strains. This loss of linearity is possibly due to the region of localised subsurface contact stress being significantly smaller than the overall experimental gauge volume, with even a minor misalignment of the gauge volume or roller position impacting the result. As the stress increases and the size of the localised stress field increases, results become more comparable with predicted values. This result was useful for determining the suitability of the applied load and selected gauge volume geometry for dynamic testing.

3.2. Time-resolved subsurface elastic strain

A long-term dynamic test was performed, with the aim of running a bearing to failure, using 'worst case' pre-overload and dynamic load conditions, as determined using FEA. An overload of $P_s = 136$ kN and a dynamic load of $P_s = 40$ kN was applied. Overall, the dynamic experiment lasted for >29 h, performing approximately 1.5 million bearing revolutions. The elastic radial strain at maximum stress, when the roller is positioned beneath the gauge volume, is presented in Fig. 9, alongside the measured SMD values. It should be noted that between 13 and 17 h there is a gap in data acquisition, as a result of the rig stalling. This resulted in the motor and support bearings being replaced as they would be the components to experience the greatest duty if the test bearing had failed. The rig was restarted and then operated for a further 12 h, until it stalled for a second time and the test was ended. A notable increase of compressive strain is observed at approximately 25 h, indicative of material softening which is frequently associated with RCF failure.

As all neutrons are detected throughout the entire experiment with the triggering signal simply acting as a time reference, cyclic strain was evaluated by segmenting the data, as described in Section 2.4. The neutron data was sorted into seven discrete time-bins, corresponding to a different point within the rollers passage, relative to bin-0, which is the point when maximum compressive strain is expected as the roller is in contact with the region of interest. Fig. 10a presents all 53 strain cycles measured over the long-term test. Each cycle has 7 data points, with
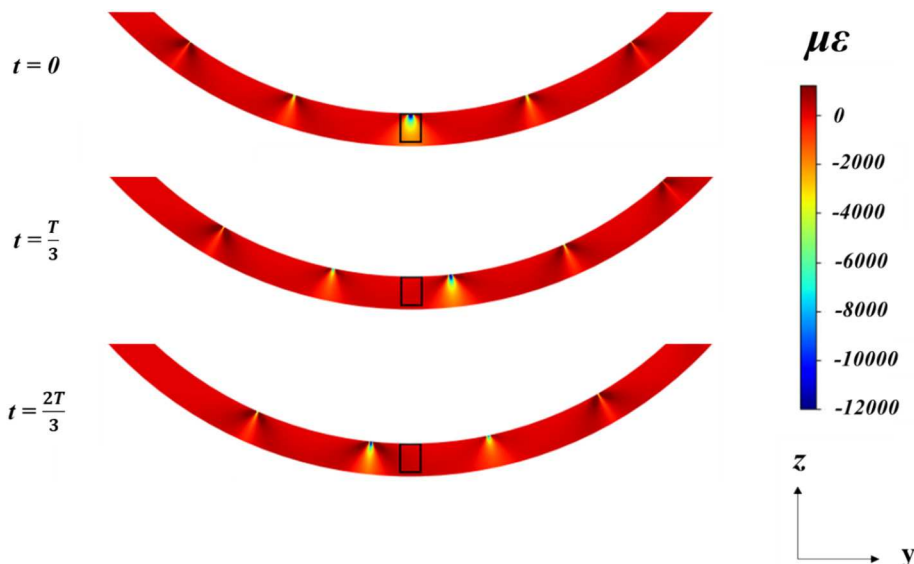

Fig. 7. Analytical model of dynamic strain in the bearing raceway at t = 0, t = T/3 and t = 2 T/3. The black box symbolises the theoretical gauge volume.
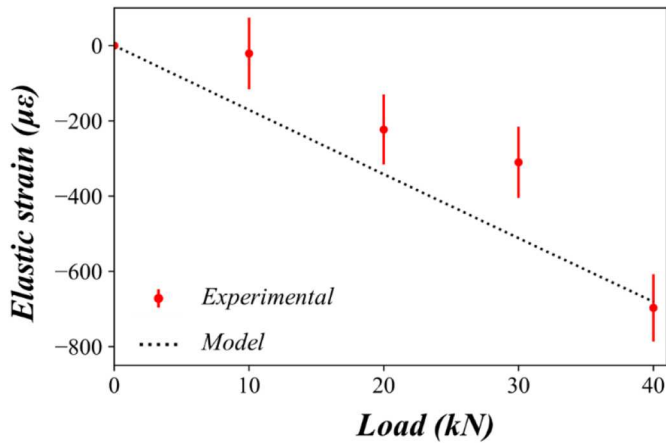
Fig. 8. Static strain for increasing load, compared to the values predicted using Hertzian contact theory.

the scan merging process offering a time resolution of slightly under 2 h per measurement.

The data is inherently noisy, as would be expected with such high frequency cyclic strain, the nature of ToF neutron data acquisition, and the time resolution being compromised by post-processing procedures. The sampling time for each cycle was intermittent relative to the absolute experimental time, yet the sample rate is constant and each cycle represents the same physical phenomena, i.e. a roller passage. Therefore, a Discrete Fourier Transform (DFT) was implemented to examine the frequency domain, in order to assess whether any periodicity existed within the strain variation [55,56]. The sample rate, f_s, was equal to the pulse width ($\Delta t = 1.08$ ms, so $f_s = 926$ Hz). This demonstrated noteworthy spikes at the BPF of 132 Hz, followed by harmonics belonging to that fundamental frequency. This gives confidence that although the data is noisy, there is an expected cyclic trend and that strain variation is consistent with the applied RCF stresses. Fig. 10b shows frequency domain from the original signal. The DFT confirming that the most prevalent frequency component related to the BPF_o, indicates that strain could be averaged for each time-bin over the entire experiment, to evaluate the overall cyclic strain variation. Fig. 11a shows the measured cyclic strain for a single roller passage as measured by neutron diffraction, compared to those predicted using the analytical raceway model, with error bars representing the standard deviation of the 53 values.

Averaging the raw signal provides strain magnitudes that are slightly lower than those predicted by modelling, and the presence of a small unexpected bump in the cyclic data. For future stroboscopic neutron experiments, it may be useful to integrate signal processing approaches for removing noise from stroboscopic data. Initially for this study, a multi-band finite impulse response filter was adopted for trialling denoising approaches, as this technique is frequently adopted in signal processing for improving signal-to-noise ratios [57,58]. The filter was used to attenuate frequencies outside of the bands; 120–150 Hz and 5–20 Hz, incorporating the BPF_o and the shaft rotational frequency, respectively. Fig. 11b shows cyclic strain results obtained from the filtered signal, demonstrating a trend more comparable to the model.

3.3. Post-mortem interrogation

3.3.1. Confocal scanning microscopy

Global plastic deformation at the contact site was visible by eye in the form of a dent, with more prominent damage close to the contact edges. To determine the extent of surface deformation a Leica DCM 3D confocal microscope with a pitch of 1.66 μm was used to examine the surface morphology in an approximately 1.86 by 8.30 mm^2 area, around the contact site. Due to limitations in the microscopes field of view, the area was divided in 24 individual scans, stitched together to produce the final 3D image, as seen in Fig. 12a. The scan confirmed that significant plastic deformation was formed, with evidence of pitting having occurred on both edges of the contact indentation.

Reference scans were also completed at a location away from the contact region, to correct for curvature of the bearing surface, allowing for examination of 2D profiles of the contact area. A profile along the x-direction, demonstrates the indentation depth along the length of the contact, shown in Fig. 12b. It appears that pitting has occurred at the contact edges, which is almost certainly due to stress concentration effects in those regions. Fig. 12c shows a profile along the y-direction taken from the edge and the middle of the contact. This also demonstrates the extent of pitting at the contact edge, with roughly a 4-times increase in depth when compared to the dent observed from the middle of the contact. Width at the centre of the contact was measured at roughly 1 mm, whilst the width during overload was 0.83 mm, as predicted using Hertzian contact theory

3.3.2. Fractography

The sample was circumferentially sectioned to observe subsurface microstructure, with a 2% nital solution used for etching. Fig. 13b demonstrates an alteration to the microstructure surrounding the contact,
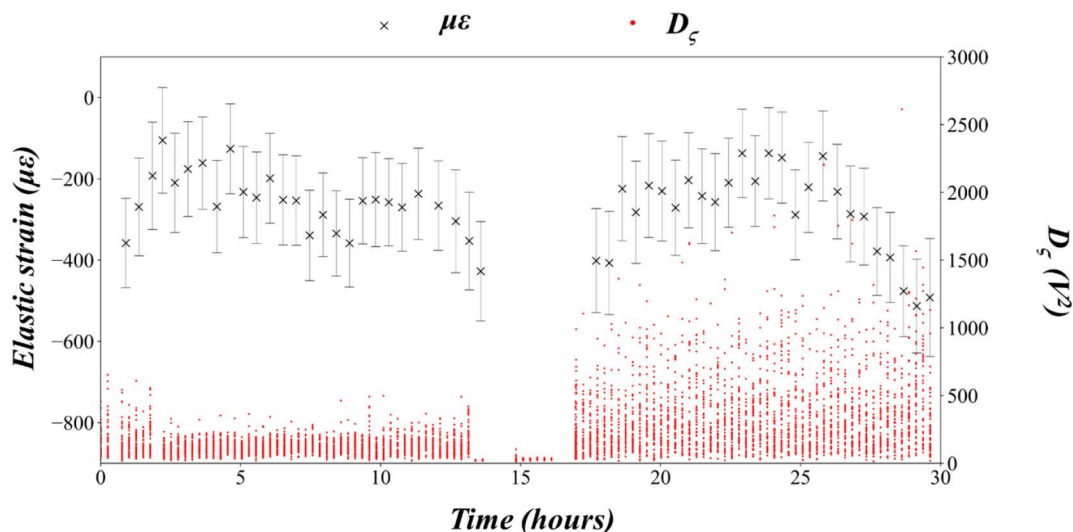

Fig. 9. Measured elastic radial strain and the Squared Mahalanobis Distance recorded over the long-term dynamic experiment.
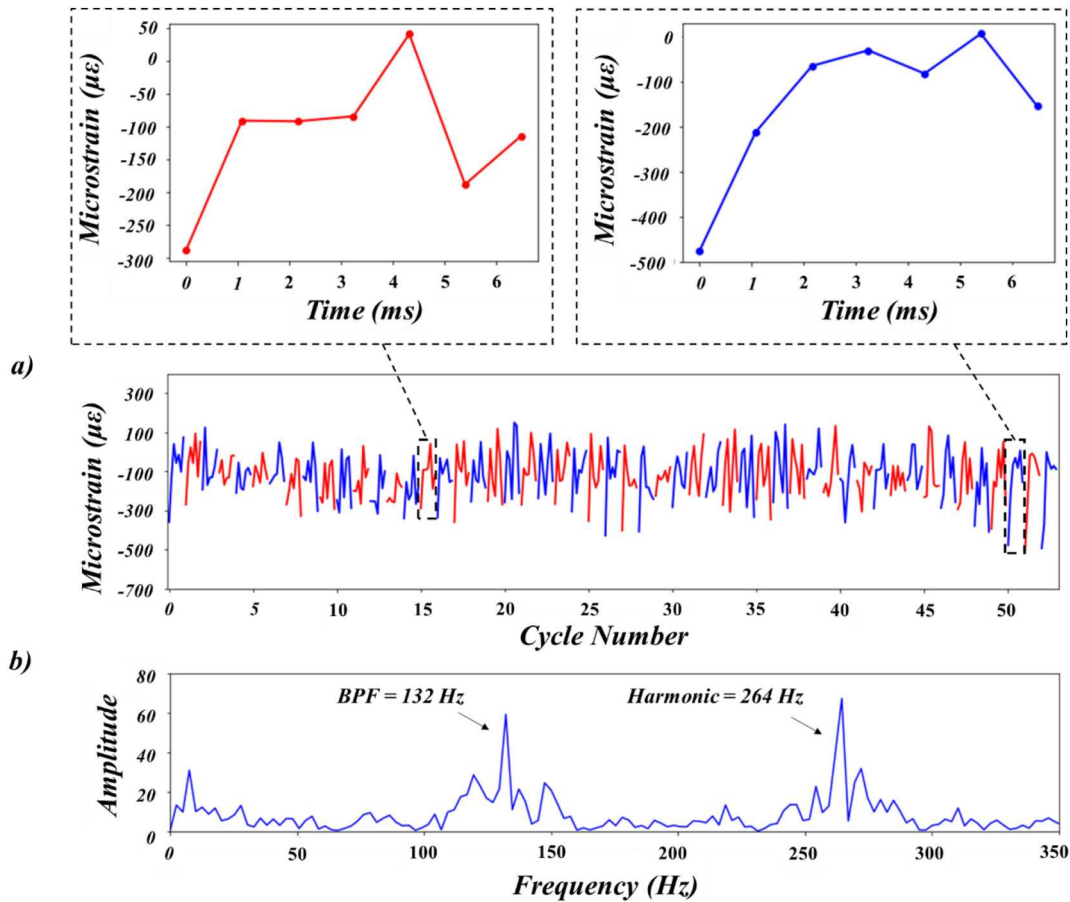
Fig. 10. (a) Calculated strain for the seven time-bins within each of the 53 dynamic cycles. Alternating colours used to provide clarity on where each cycle begins and ends. INSET: two examples of individual cycles represented on the time axis (b) Frequency domain of the 53 cycles, under the assumption the data is continuous. (For interpretation of the references to colour in this figure legend, the reader is referred to the web version of this article.)

with WEA's close to the surface and a substantial DER that gradually brightens as it fades into the original microstructure with increasing subsurface depth. The darkest DER appears as a band, running between the surface and a depth of roughly 170 μm, closely associated with a maximum shear stress at the depth of 175 μm, predicted using Hertzian contact theory and indicated using a dashed red line. Fig. 13c demonstrates a subsurface region that contained a WEC, surrounded by WEA, appearing to initiate at an inclusion, typical of WECs [14]. The crack was observed at a depth of 120 μm into the subsurface. Fig. 13d shows a section whereby there was evidence of DER, close to several WEA formations around potential cracks or material voids.

3.4. Offline bearing fatigue

A separate offline fatigue experiment, where a different test bearing and without diffraction capabilities, was performed with the FRLF and an Instron loading frame, under the same overload ($P_s = 136$ kN) and dynamic loading ($P_s = 40$ kN) conditions, for an equivalent of approximately 0.28 million revolutions. Considering the statistical nature of bearing failure, this is judged to be within reasonable range of the failure observed during the neutron experiment. A large axial crack had formed, with most severe damage appearing in the subsurface beneath the contact edges. Microstructure, observed using a scanning electron
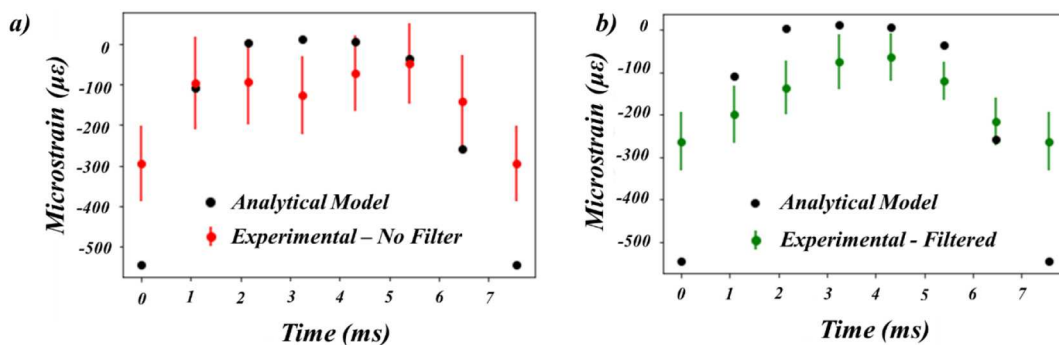

Fig. 11. (a) The average experimental strain at each time within the 53 recorded cycles, compared to the strain predicted by the analytical raceway model. (b) The average experimental strain, post filtering, at each time within the 53 recorded cycles, compared to the model. Error bars represent the standard deviation. Please note that the final point for both (a) and (b) is a repeat of $t = 0$ s, completing an entire cycle.
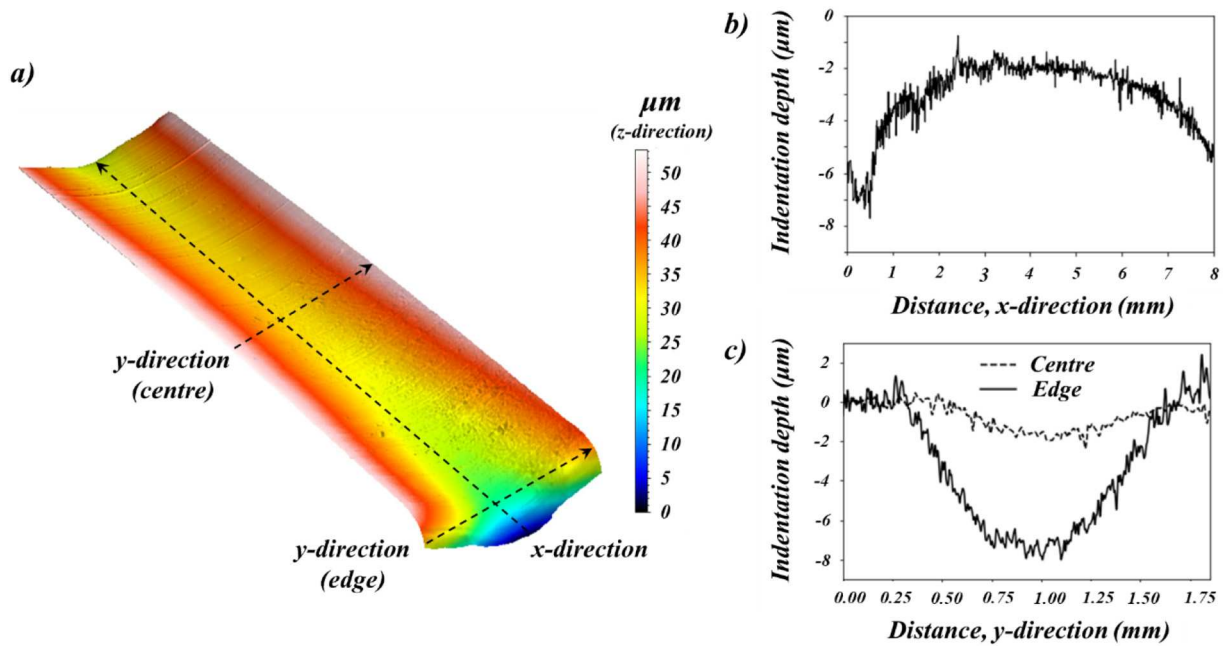
Fig. 12. (a) Three-dimensional representation of the contact site generated using a confocal scanning microscopy. (b) Profile of the contact depth along the x-direction. (c) Profile of the contact depth along the y-direction, for both the centre and edge of the contact.

microscope (SEM), appears typical of ductile fatigue, with striations occurring perpendicular to the subsurface crack, in the same region where clear WEA has formed, as seen with the optical microscope. Fig. 14 shows the axial cross sections, observed using SEM and optical microscopy from the FRLF test.

4. Discussion

During the dynamic test, a significant increase in the measured compressive strain begins shortly after the initial interruption to rig operation at 13 h, suggesting that test bearing failure might have prevented the rig from functioning correctly. The proposed test bearing failure, along with support bearing degradation, would have increased the coefficient of friction, resulting in the required torque exceeding that being provided by the motor. Assuming that bearing failure had occurred when the rig initially stalled at 13 h, this corresponds to a 59% reduction of life, compared to the expected L_{10} prediction for that applied load.

For the first time, a stroboscopic diffraction procedure has been used, simultaneously with condition monitoring techniques, and has successfully identified an approximate time of failure. Multivariate analysis using the novelty detection method on vibration levels, revealed a statistically significant increase in SMD values after recommencing rig operation, relative to standard operating conditions, suggesting damage had been initiated (as seen in Fig. 9). A further investigation on damage localisation was performed in parallel by Martinez et al. [45], where a localisation approach used time-delay and sum beamforming methods with three AE sensors. This indicated that the detected abnormality originated from the overloaded site, with standard deviation uncertainty of 45.2°. Nonetheless, bearing failure is defined as the point at which it no longer operates as intended, which is certainly implied by these non-destructive techniques [59].

The proposed stroboscopic technique offers a novel method for further understanding tribological mechanisms, such as rolling contact fatigue, with its ability to non-destructively measure dynamic strain using neutron diffraction. This is comparable with other diffraction techniques, for example using synchrotron X-rays. A previous experiment, performed with energy dispersive X-ray diffraction, using the same rig and test bearing, had previously measured radial strain stroboscopically in a dynamically loaded sample [40]. A benefit of using X-ray diffraction

is the improved spatial and temporal resolution, with the mentioned experiment obtaining strain values within 13 min, in addition to a gauge volume cross-sectional area of only $150 \times 150 \ \mu m^2$. The results indicated similar effects on elastic strain, with gradually increasing compressive strain prior to an observed failure. It was also proposed that this effect was the result of a reduction in yield strength due to material softening, induced during severe plastic deformation. The consequence of this damage is accelerated onset of rolling contact fatigue associated instability (Phase III), supporting the hypothesis that overloads significantly reduce bearing life expectancy.

Whilst spatial and temporal resolution are better for synchrotron X-ray diffraction, neutron diffraction holds the unique capability for characterising cyclic strains, as every detected neutron can be utilised. Additionally, neutron diffraction is better suited for probing engineering materials of larger geometries, more representative of commercial components. For neutron diffraction, strain measurement uncertainties were greater for dynamic scans compared to static scans, although this was not the case for X-ray experiments, where signal-to-noise was similar for both static and dynamic measurements. Prior to this study, data analysis procedures for stroboscopic neutron techniques were not practical; however significant developments in the post-processing of eventmode data have been demonstrated by this work.

Examining the bearing post-mortem offers the proposal that failure could either be related to surface damage, subsurface damage or a combination of both. Pre-overloading certainly appears to have accelerated bearing failure via surface denting prior to the dynamic test, yet there is also evidence to suggest subsurface failure as a failure mode. The overload seems to have contributed towards surface indentation exaggerated at the contact edges by stress concentration of cyclic loading. In addition, the subsurface plastic deformation appears to have generated a region prone to subsurface cracking. The DER appears to resemble the shape associated with a Hertzian contact, of similar size to the predicted plastic zone generated during pre-overloading, as seen in Fig. 13b. It has been demonstrated in previous studies that DER's resemble the size and shape of plastically deformed microstructure, as predicted by elastoplastic modelling [20]. It has been proposed that DER occurs prior to the formation of WEC and WEA, with Fig. 13 demonstrating WEA growth in the region closest to the subsurface, within the DER [60]. It is not within the scope of this work to characterise the exact
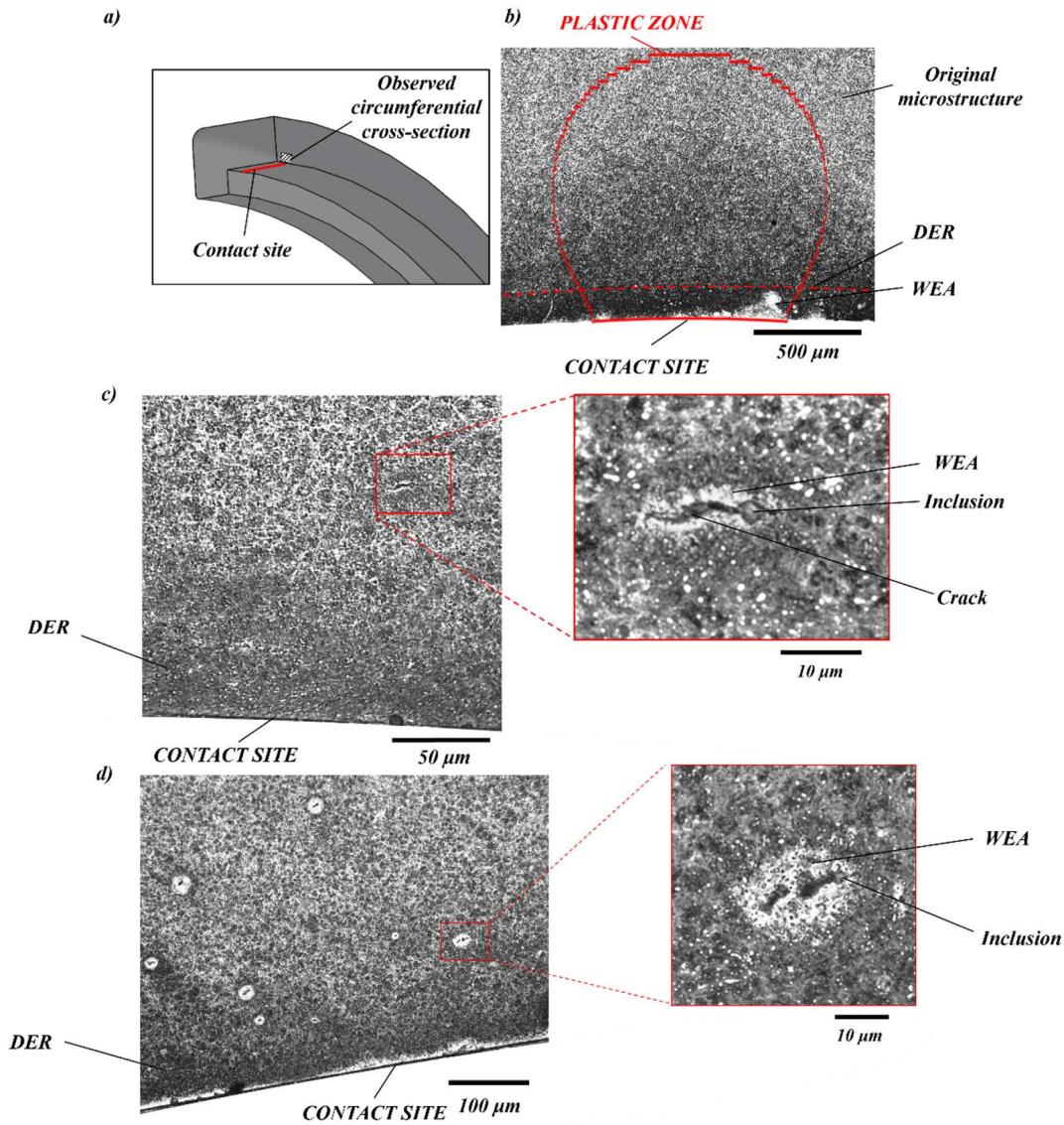
Fig. 13. (a) Schematic to demonstrate the circumferential cross-section being observed. (b) Subsurface image in the overloaded region. (c) Subsurface crack initiated at a material inclusion, with associated WEA. (d) Subsurface damage and WEA, adjacent to a material inclusion.

cause of failure, yet condition monitoring approaches confirmed damage propagation at the contact site, stimulated during RCF cycling. The offline experiment performed using the FRLF supports the confocal microscopy results described in Section 3.3, as the most detrimental pitting depths were greatest at the contact edges and acting as a location of higher failure probability. Stress concentration effects are proposed as the probable cause for increased damage at the contact edges.

Now that first experiments using stroboscopic strain measurements with roller bearings have been successfully conducted on the ENGIN-X neutron diffractometer, the technique could be scaled-up to study full-size commercial WTG bearings. The high penetration power of neutrons can pass through up to 60 mm of steel, with high speed shaft bearings having raceway thicknesses of approximately 48 mm [25,61]. Using larger test bearings would generate localised stress fields with significantly larger dimensions, improving accuracy as the gauge volume size would be more suitable and allow for characterisation of greater strain magnitudes. Additionally, reducing the bearing rotational speed would allow for either a greater number of time-bins per cycle, or increased pulse widths, reducing the number revolutions necessary to acquire sufficient fitting statistics. However, slowing the bearing would require longer experimental times to complete a similar number of revolutions, which is not always possible for neutron diffraction

experiments, as the designated beamtime is usually no longer than a few days. This work demonstrated the potential of stroboscopic techniques to measure cyclic strain at loading frequencies of approximately 132 Hz, whereas in previous studies cycling rates have generally been much slower, for example 0.5 Hz [32,33]. It was apparent that accuracy can be hindered at such high frequencies, which is to be expected for a ToF technique. Therefore, it is proposed that there is considerable scope for the future development of more advanced digital signal processing techniques for analysing stroboscopic data, collected under rapidly varying cyclic stress conditions.

5. Conclusions

- A custom-built rig and fibre optic triggering system permitted measurement of time-resolved strain using a novel approach to stroboscopic neutron diffraction.
- Static measurements demonstrated closest agreement with Hertzian contact predictions at high loads.
- During a long-term dynamic scan, a condition monitoring novelty detection technique was able to identify bearing failure. Subsequently, a significant increase in subsurface compressive radial strain was observed, as measured using stroboscopic neutron diffraction.
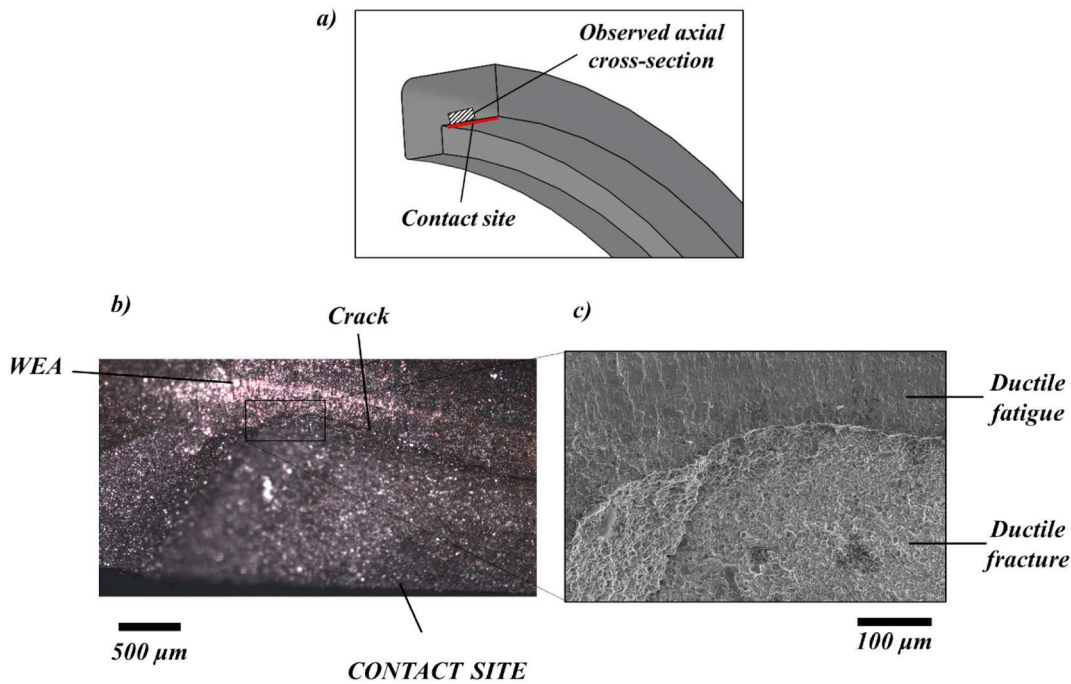
Fig. 14. (a) Schematic to demonstrate the axial cross-section being observed. (b) Optical microscope image of the contact edge subsurface. (c) SEM image of the contact edge subsurface.

- Cyclic strain associated with rolling contact fatigue was measured using every detected neutron. This was possible due to stroboscopic pulses from the rig and neutron detection events being synchronised.
- Post-mortem surface scans and mechanical cross-sectioning show that the contact edge is the most probable failure location yet was unable to confirm whether failure occurred at the surface or in the subsurface.

CRediT authorship contribution statement

M. Marshall: Conceptualization, Methodology, Resources, Writing - review & editing, Supervision, Project administration, Funding acquisition.**I. Martinez:**Methodology, Investigation, Formal analysis, Software, Validation, Data curation.**S. Moorby:**Resources.**T. Connolley:**Resources, Conceptualization, Supervision, Project administration.**M. Mostafavi:** Conceptualization, Methodology, Resources, Writing - review & editing, Supervision, Project administration, Funding acquisition.**S. Kabra:**Conceptualization, Methodology, Resources, Writing - review & editing, Supervision, Project administration, Funding acquisition, Data curation.

Declaration of competing interest

The authors declare that they have no known competing financial interests or personal relationships that could have appeared to influence the work reported in this paper.

Data availability

All data is available with the corresponding author and provided upon request.

References

[1] International Renewable Energy Agency (IRENA), Renewable Capacity Statistics 2018, 2018.
[2] D.H.M. de Azevedo, A.M. Araújo, N. Bouchonneau, A review of wind turbine bearing condition monitoring: state of the art and challenges, Renew. Sust. Energ. Rev. 56 (2016) 368–379.
[3] H. Chengbing, F. Xinxin, Institutions function and failure statistic and analysis of wind turbine, Phys. Procedia 24 (2012) 25–30.
[4] W. Qiao, S. Member, D. Lu, S. Member, A survey on wind turbine condition monitoring and fault diagnosis — part I: components and subsystems, IEEE Trans. Ind. Electron. 62 (10) (2015) 6536–6545.
[5] Y. Guo, J. Keller, W. LaCava, Planetary gear load sharing of wind turbine drivetrains subjected to non-torque loads, Wind Energy 18 (2015) 757–768.
[6] J.S. Nam, Y.J. Park, S.J. Jo, H.S. Kim, S.B. Shim, Development of a gearbox test rig with non-torque loading capacity, J. Mech. Sci. Technol. 30 (4) (2016) 1713–1722.
[7] H. Long, R.S. Dwyer-Joyce, T. Bruce, Dynamic modelling of wind turbine gearbox bearing loading during transient events, IET Renew Power Gener 9 (7) (2015) 821–830.
[8] N.T. Garabedian, B.J. Gould, G.L. Doll, D.L. Burris, The cause of premature wind turbine bearing failures: overloading or underloading? Tribol. Trans. 61 (5) (2018) 850–859.
[9] M.H. Evans, White structure flaking (WSF) in wind turbine gearbox bearings: effects of "butterflies" and white etching cracks (WECs), Mater. Sci. Technol. 28 (1) (2012) 3–22.
[10] A. Reid, I. Martinez, M. Marshall, T. Minniti, S. Kabra, W. Kockelmann, T. Connolley, M. Mostafavi, Mapping of axial plastic zone for roller bearing overloads using neutron transmission imaging, Mater. Des. 156 (2018) 103–112.
[11] C.R. Gagg, P.R. Lewis, Wear as a product failure mechanism — overview and case studies, Eng. Fail. Anal. 14 (2007) 1618–1640.
[12] A.D. Richardson, M. Evans, L. Wang, M. Ingram, Z. Rowland, G. Llanos, R.J.K. Wood, The effect of over-based calcium sulfonate detergent additives on white etching crack (WEC) formation in rolling contact fatigue tested 100Cr6 steel, Tribology Int. 133 (2019) 246–262.
[13] B. Gould, M. Paladugu, N.G. Demas, A.C. Greco, R.S. Hyde, Figure the impact of steel microstructure and heat treatment on the formation of white etching cracks, Tribology Int 134 (2019) 232–239.
[14] M. Evans, An updated review: white etching cracks (WECs) and axial cracks in wind turbine gearbox bearings, Mater. Sci. Technol. 32 (11) (2016) 1133–1169.
[15] T. Bruce, E. Rounding, H. Long, R.S. Dwyer-Joyce, Characterisation of white etching crack damage in wind turbine gearbox bearings, Wear 338–339 (2015) 164–177.

[16] A. Greco, S. Sheng, J. Keller, A. Erdemir, Material wear and fatigue in wind turbine systems, Wear 302 (1–2) (2013) 1583–1591.

[17] H.K.D.H. Bhadeshia, H.K.D.H. Bhadeshia, Critical assessment 13: elimination of white etching matter in bearing steels, Mater Sci Technol ISSN 31 (9) (2015) 1011–1015.

[18] B. Gould, A. Greco, The influence of sliding and contact severity on the generation of white etching cracks, Tribol. Lett. 60 (29) (2015) 1–13.

[19] J. Gegner, Tribological aspects of rolling bearing failures, Tribology – Lubricants and Lubrication, IntechOpen 2011, pp. 33–94.

[20] L. Xie, D. Palmer, F. Otto, Z. Wang, Q.J. Wang, L. Xie, D. Palmer, F. Otto, Z. Wang, Effect of surface hardening technique and case depth on rolling contact fatigue behavior of alloy steels, Tribol. Trans. 58 (2) (2015) 215–224.

[21] M.T. Hutchings, P.J. Withers, T.M. Holden, T. Lorentzen, Introduction to the Characterization of Residual Stress by Neutron Diffraction, CRC Press, Boca Raton, FL, 2005.

[22] P.J. Withers, H.K.D.H. Bhadeshia, Residual stress Part 1 – Measurement techniques, Mater. Sci. Technol. 17 (2001) 355–365.

[23] M.W. Johnson, M.R. Daymond, An optimum design for a time-of-flight neutron diffractometer for measuring engineering stresses, J. Appl. Crystallogr. 35 (2002) 49–57.

[24] P.J. Withers, P.J. Webster, Neutron and synchrotron X-ray strain scanning, Strain 37 (1) (2001) 19–33.

[25] J.R. Santisteban, M.R. Daymond, J.A. James, L. Edwards, ENGIN-X: a third-generation neutron strain scanner, J. Appl. Crystallogr. 39 (6) (2006) 812–825.

[26] G.S. Pawley, Unit-cell refinement from powder diffraction scans, J. Appl. Crystallogr. 14 (1981) 357–361.

[27] P. Scardi, L.B. Mccusker, D.R.B. Von, D.E. Cox, D. Loue, Rietveld refinement guidelines, J. Appl. Crystallogr. 32 (1999) 36–50.

[28] G. Salerno, C. Bennett, W. Sun, A. Becker, N. Palumbo, J. Kelleher, On the interaction between welding residual stresses: a numerical and experimental investigation, Int. J. Mech. Sci. 144 (2018) 654–667.

[29] C. Bühr, B. Ahmad, P.A. Colegrove, A.R. Mcandrew, H. Guo, X. Zhang, Prediction of residual stress within linear friction welds using a computationally efficient modelling approach, Mater. Des. 139 (2018) 222–232.

[30] A. Narayanan, M. Mostafavi, T. Pirling, S. Kabra, R. Lewis, M.J. Pavier, M.J. Peel, Residual stress in laser cladded rail, Tribology Int. 140 (2019), 105844.

[31] W. Woo, E. Huang, J. Yeh, H. Choo, C. Lee, S. Tu, In-situ neutron diffraction studies on high-temperature deformation behavior in a CoCrFeMnNi high entropy alloy, Intermetallics 62 (2015) 1–6.

[32] P.S. Van, J. Wagner, T. Panzner, M.V. Upadhyay, T.T.T. Trang, S.H. Van, In-situ neutron diffraction during biaxial deformation, Acta Mater. 105 (2016) 404–416.

[33] Z. Wang, A.D. Stoica, D. Ma, A.M. Beese, Stress relaxation in a nickel-base superalloy at elevated temperatures with in situ neutron diffraction characterization: application to additive manufacturing, Mater. Sci. Eng. A 714 (2018) 75–83.

[34] H. Wang, W. Woo, S. Yeol, G. An, D. Kim, Correlation of localized residual stresses with ductile fracture toughness using in situ neutron diffraction and finite element modelling, Int. J. Mech. Sci. 160 (2019) 332–342.

[35] M.R. Daymond, P.J. Withers, New stroboscopic neutron diffraction method for monitoring materials subjected to cyclic loads: thermal cycling of metal matrix composites, Scr. Mater. 35 (6) (1996) 717–720.

[36] J. Feuchtwanger, P. Lázpita, N. Vidal, J.M. Barandiaran, J. Gutiérrez, T. Hansen, M. Peel, C. Mondelli, R.C. O'Handley, S.M. Allen, Rearrangement of twin variants in ferromagnetic shape memory alloy–polyurethane composites studied by stroboscopic neutron diffraction, J Phys Condens Matter 20 (10) (2008), 104247.

[37] T. Kawasaki, Y. Inamura, T. Ito, T. Nakatani, Stroboscopic time-of-flight neutron diffraction during cyclic testing using the event data recording research papers, J. Appl. Crystallogr. 51 (2018) 630–634.

[38] N. Baimpas, M. Drakopoulos, T. Connolley, X. Song, C. Pandazaras, A.M. Korsunsky, A feasibility study of dynamic stress analysis inside a running internal combustion engine using synchrotron X-ray beams, J. Synchrotron Radiat. 20 (2) (2013) 316–323.

[39] M. Mostafavi, D.M. Collins, M.J. Peel, C. Reinhard, S.M. Barhli, R. Mills, M.B. Marshall, R.S. Dwyer-Joyce, T. Connolley, Dynamic contact strain measurement by time-resolved stroboscopic energy dispersive synchrotron X-ray diffraction, Strain 53 (2) (2017) 1–13.

[40] A. Reid, C. Simpson, I. Martinez, S. Kabra, T. Connolley, O. Magdysyuk, C. Charlesworth, M. Marshall, M. Mostafavi, Measurement of strain evolution in overloaded roller bearings using energy dispersive X-ray diffraction, Tribiology Int. 140 (2019), 105893.

[41] H.K.D.H. Bhadeshia, Steels for bearings, Prog. Mater. Sci. 57 (2012) 268–435.

[42] Y.B. Guo, C.R. Liu, Mechanical properties of hardened AISI 52100 steel in hard machining processes, J. Manuf. Sci. Eng. 124 (1) (2002) 1–9.

[43] M. Drakopoulos, T. Connolley, C. Reinhard, R. Atwood, O. Magdysyuk, N. Vo, M. Hart, L. Connor, B. Humphreys, G. Howell, S. Davies, T. Hill, G. Wilkin, U. Pedersen, A. Foster, N. De Maio, M. Basham, F. Yuan, K. Wanelik, I12: the joint engineering, environment and processing (JEEP) beamline at diamond light source, J. Synchrotron Radiat. 22 (2015) (2015) 828–838.

[44] V.V.F. Sears, Neutron scattering lengths and cross sections, Neutron News 3 (3) (1992) 26–37.

[45] I. Martinez, A. Reid, M. Marshall, R. Dwyer-Joyce, G. Manson, Acoustic Emission Localisation on Roller Bearing Defects Using Time-Delay and Sum Beamforming Technique, UNPUBLISHED 2019.

[46] M.S. Patil, J. Mathew, P.K. Rajendrakumar, S. Desai, A theoretical model to predict the effect of localized defect on vibrations associated with ball bearing, Int. J. Mech. Sci. 52 (9) (2010) 1193–1201.

[47] O. Arnold, J.C. Bilheux, J.M. Borreguero, A. Buts, S.I. Campbell, L. Chapon, M. Doucet, N. Draper, R.F. Leal, M.A. Gigg, V.E. Lynch, A. Markvardsen, D.J. Mikkelson, R.L. Mikkelson, R. Miller, K. Palmen, P. Parker, G. Passos, T.G. Perring, et al., Mantid — data analysis and visualization package for neutron scattering and μ SR experiments, Nucl. Inst. Methods Phys. Res. A 764 (2014) 156–166.

[48] B.H. Toby, R.B.V. Dreele, GSAS-II: The Genesis of a Modern Open-Source all Purpose Crystallography Software Package, 2013 544–549.

[49] DSS, ABAQUS Analysis User's Manual 6.14–2, DSS (Dassault Systèmes Simulia Corp), 2014.

[50] ASM International, Atlas of Stress-Strain Curves, ASM International, 2002.

[51] J. Williams, Engineering Tribology, Cambridge University Press, 2005.

[52] K.L. Johnson, K.L. Johnson, Contact Mechanics, Cambridge University Press, 1987.

[53] J.A. Williams, R.S. Dwyer-Joyce, Contact between solid surfaces, Modern Tribology Handbook 2001, pp. 121–162.

[54] M. Guessasma, C. Machado, Three-dimensional DEM Modelling of ball bearing with lubrication regime prediction, Lubricants 6 (2018) 46.

[55] B.J.W. Cooley, J.W. Tukey, An algorithm for the machine calculation complex Fourier series, Math. Comput. 19 (90) (1965) 297–301.

[56] J.F. James, A Student's Guide to Fourier Transforms: With Applications in Physics and Engineering, Cambridge University Press, 2011.

[57] P.S.R. Diniz, S. Da, A.B. Eduardo, S.L. Netto, Digital Signal Processing: System Analysis and Design, Cambridge University Press, 2010.

[58] S. De Ridder, X. Neyt, N. Pattyn, P. Migeotte, Comparison between EEMD, wavelet and FIR Denoising: influence on event detection in impedance cardiography, 2011 Annual International Conference of the IEEE Engineering in Medicine and Biology Society 2011, pp. 806–809.

[59] T.A. Harris, M.N. Kotzalas, Essential Concepts of Bearing Technology: Rolling Bearing Analysis, CRC Press, 2006.

[60] V. Šmelova, A. Schwedt, L. Wang, W. Holweger, J. Mayer, Microstructural changes in white etching cracks (WECs) and their relationship with those in dark etching region (DER) and white etching bands (WEBs) due to rolling contact fatigue (RCF), Int J Fatigue J 100 (2017) 148–158.

[61] G. Nicholas, T. Howard, R. Dwyer-Joyce, J. Wheals, D. Benchebra, Direct load measurement of a wind turbine high speed shaft bearing in the field, 1st World Congress on Condition Monitoring 2017, pp. 879–886.